

Fully Depleted Ti–Nb–Ta–Zr–O Nanotubes: Interfacial Charge Dynamics and Solar Hydrogen Production

Yi-Hsuan Chiu,^{†,‡} Ting-Hsuan Lai,[†] Chun-Yi Chen,^{*,‡,§} Ping-Yen Hsieh,[†] Kazunari Ozasa,^{||} Mitsuo Niinomi,[⊥] Kiyoshi Okada,[‡] Tso-Fu Mark Chang,^{*,‡,§} Nobuhiro Matsushita,[△] Masato Sone,^{‡,§} and Yung-Jung Hsu^{*,†,ⓑ}

[†]Department of Materials Science and Engineering, National Chiao Tung University, Hsinchu 30010, Taiwan

[‡]Institute of Innovative Research, Tokyo Institute of Technology, 4259 Nagatsuta-cho, Midori-ku, Yokohama 226-8503, Japan

[§]CREST, Japan Science and Technology Agency, 4259 Nagatsuta-cho, Midori-ku, Yokohama 226-8503, Japan

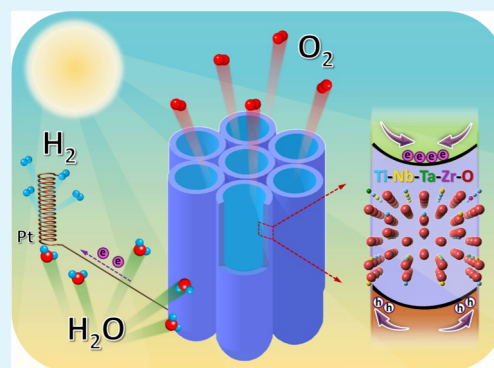
^{||}Bioengineering Lab, RIKEN, 2-1 Hirosawa, Wako, Saitama 351-0198, Japan

[⊥]Institute for Materials Research, Tohoku University, 2-1-1 Katahira, Aoba-ku, Sendai 980-8577, Japan

[△]Department of Materials Science and Engineering, Tokyo Institute of Technology, 2-12-1 Ookayama, Meguro-ku, Tokyo 152-8552, Japan

ABSTRACT: Poor kinetics of hole transportation at the electrode/electrolyte interface is regarded as a primary cause for the mediocre performance of n-type TiO₂ photoelectrodes. By adopting nanotubes as the electrode backbone, light absorption and carrier collection can be spatially decoupled, allowing n-type TiO₂, with its short hole diffusion length, to maximize the use of the available photoexcited charge carriers during operation in photoelectrochemical (PEC) water splitting. Here, we presented a delicate electrochemical anodization process for the preparation of quaternary Ti–Nb–Ta–Zr–O mixed-oxide (denoted as TNTZO) nanotube arrays and demonstrated their utility in PEC water splitting. The charge-transfer dynamics for the electrodes was investigated using time-resolved photoluminescence, electrochemical impedance spectroscopy, and the decay of open-circuit voltage analysis. Data reveal that the superior photoactivity of TNTZO over pristine TiO₂ originated from the introduction of Nd, Ta, and Zr elements, which enhanced the amount of accessible charge carriers, modified the electronic structure, and improved the hole injection kinetics for expediting water splitting. By modulating the water content of the electrolyte employed in the anodization process, the wall thickness of the grown TNTZO nanotubes can be reduced to a size smaller than that of the depletion layer thickness, realizing a fully depleted state for charge carriers to further advance the PEC performance. Hydrogen evolution tests demonstrate the practical efficacy of TNTZO for realizing solar hydrogen production. Furthermore, with the composition complexity and fully depleted band structure, the present TNTZO nanotube arrays may offer a feasible and universal platform for the loading of other semiconductors to construct a sophisticated heterostructure photoelectrode paradigm, in which the photoexcited charge carriers can be entirely utilized for efficient solar-to-fuel conversion.

KEYWORDS: Ti–Nb–Ta–Zr–O, nanotube arrays, solar water splitting, fully depleted, interfacial charge dynamics



1. INTRODUCTION

Research on the nanoscale control of functional materials has found a huge surge over the past decade because it affords the opportunity to attain a wide range of sensational material properties, which are improbable to acquire from the bulk. In this regard, electrochemical anodization is considered a particularly feasible approach for obtaining nanostructures with tailored architectures, especially highly oriented nanotube arrays. Self-organized nanotube arrays may overcome the drawbacks of nanoparticle films relating to interfacial disorder and structural defects; besides, they exhibit the distinct advantages of high surface area and oriented charge transfer, providing great potential for various kinds of energy conversion

and storage applications, for instance, dye-sensitized solar cells,¹ photoelectrochemical (PEC) water splitting,² photocatalytic hydrogen evolution,³ dye photodegradation,⁴ and batteries and electrochemical capacitors.⁵ PEC water splitting capable of producing solar hydrogen represents an elegant solution to the future global energy problems. The structural one-dimensionality inherent to nanotubes has been widely employed to design photoelectrodes for versatile PEC systems that exploit the anisotropic geometric features to increase the availability of

Received: January 15, 2018

Accepted: April 17, 2018

Published: April 17, 2018

charge carriers.^{6,7} Importantly, the spatial decoupling of light absorption from the carrier collection rendered by the nanotube geometry is a principal advantage for PEC reactions. Thus far, many efforts have been devoted to utilizing semiconductor nanotube arrays as versatile photoelectrode platforms for realizing PEC water splitting.^{8–15}

As one of the most ancient functional materials investigated in science, n-type TiO₂ is attracting increasing attention with emerging nanotechnology, especially in the aspect of PEC water splitting. However, the utility of pristine TiO₂ as a photoelectrode is limited by the intrinsically slow charge transfer and prevalent charge recombination. The poor kinetics of hole transportation at the electrode/electrolyte interface is regarded as a primary cause for the mediocre PEC performance of TiO₂.¹⁶ Note that the hole diffusion length of TiO₂ is approximately 10 nm,^{17,18} confining the effective area of charge carrier generation and collection to the near-surface region. By adopting nanotubes as the electrode backbone, light absorption and carrier collection can be spatially decoupled, enabling the former to proceed along the longitudinal tube axis and the latter to follow the radial direction. In an ideal scenario, the nanotubes can be prepared with a tube length sufficient for maximizing the photon absorption and at the same time, possessing considerably thin wall thicknesses to ensure effective charge injection into the electrolyte. The nanotube geometry can therefore allow TiO₂, with its short hole diffusion length, to utilize most of the photoexcited charge carriers. On the other hand, modification of band structure by means of metal particle decoration,^{19–21} secondary semiconductor introduction,^{9,22–24} foreign element doping,^{10,11,25–29} and mixed-oxide formation^{30–32} has been widely implemented for TiO₂ to advance its carrier utilization and thereby improve the PEC performance. Among the different approaches, structural mixing with foreign elements or other oxides is especially appealing for enhancing the photoactivity of TiO₂ because the synergistic effect may operate. These developments have witnessed an intense demand for structurally and electronically modifying TiO₂ photoelectrodes to reach the criteria of conducting PEC solar water splitting.

In this work, we developed a delicate electrochemical anodization process for the preparation of quaternary titanium-based mixed-oxide nanotube arrays and demonstrated their utility in PEC water splitting. The synthesis was carried out by performing anodization on a Ti₂₉Nb₁₃Ta_{4,6}Zr alloy at a constant voltage in the fluoride-containing ethylene glycol electrolyte, which led to the self-organization of Ti–Nb–Ta–Zr–O mixed-oxide (denoted as TNTZO) nanotubes. TNTZO alloys have been widely used for biomedical applications by virtue of their excellent biocompatibility and in vivo bioactivity.³³ Compared with the binary titanium alloys, the quaternary TNTZO may exhibit superior synergistic properties owing to the inherently higher degree of complexity.³⁴ Particularly, the practical use of TNTZO toward PEC solar water splitting has never been addressed. Because of the composition complexity, TNTZO possesses many fascinating features propitious to PEC applications. For the TNTZO, the introduced Nb, Ta, and Zr can induce shallow donor states to increase the carrier concentration and simultaneously suppress trap-state formation, promoting effective charge transfer.^{35–39} Because the merits of each component can be incorporated, the TNTZO nanotube arrays exhibited superior PEC photoactivity over that of pristine TiO₂ under AM 1.5G illumination, demonstrating their promise as an alternative, practical

photoelectrode candidate. The intriguing photoactive nature of TNTZO nanotubes was further examined by studying the interfacial charge dynamics with time-resolved photoluminescence (PL), electrochemical impedance spectroscopy (EIS), and the decay of open-circuit voltage (V_{oc}) analysis. By modulating the water content of electrolyte for anodization, the wall thickness of the grown TNTZO can be reduced to a size smaller than the depletion layer thickness, leading to a fully depleted state for charge carriers to advance the PEC performance. The fully depleted TNTZO nanotubes may serve as a versatile structural backbone for the loading of other semiconductors, allowing the construction of a sophisticated heterostructure photoelectrode paradigm for efficient solar-to-fuel conversion.

2. EXPERIMENTAL SECTION

2.1. Anodization Growth of TNTZO. Bulk alloy rods with nominal compositions of Ti₂₉Nb₁₃Ta_{4,6}Zr were prepared with a powder metallurgical method consisting of induction skull melting, hot forging, and post-annealing. A spark erosion wire was then used to cut the bulk alloy rods into thin alloy plates (1.0 cm × 1.0 cm × 0.2 cm). Prior to anodization, these alloy plates were polished using 4000-grit SiC papers and cleansed by sonication with acetone, ethanol, and deionized water. A customized two-electrode cell was employed to conduct electrochemical anodization at 20 V. The alloy plate was used as the working electrode, whereas a Pt foil (1.0 cm × 2.0 cm) was used as the counter. The supporting electrolyte was prepared by mixing the NH₄F-containing (0.3 wt %) ethylene glycol solution with a given content of deionized water. Upon anodization, the samples were gently rinsed using deionized water and allowed for annealing treatment in air at 500 °C for 3 h. In this work, the amount of water added to the electrolyte was varied (20, 10, 0.9 vol %) to obtain TNTZO with different geometric features. The resulting samples were, respectively, denoted as TNTZO-1, TNTZO-2, and TNTZO-3. For comparison purpose, we also prepared for pristine TiO₂ nanotube arrays by conducting the same anodization treatment on the Ti foils (2 cm × 2 cm × 0.3 cm, 99.95% in purity).

2.2. PEC Measurements. The experimental procedures of conducting PEC measurements followed those reported in the previous works.^{40,41} A quartz-windowed cell, comprising a Ag/AgCl electrode (saturated KCl) as a reference and a Pt foil as the counter, was configured for measurements. The electrolyte was composed of NaOH aqueous solution (1.0 M, pH = 13.9). The photoanodes were assembled by attaching a copper cable to the conductive part on the sample surface, followed by jointing using Ag conducting paint and epoxy. The illumination source was provided by a xenon lamp (Newport, LCS-100, 94011A) coupled with an AM 1.5G filter, giving a 1 sun illumination of 100 mW cm⁻². All of the PEC data including linear-sweep voltammograms (I – V curves) and chronoamperometry scans (I – t curves) were recorded from a potentiostat (Solartron 1287A) equipped with a 1252A frequency response analyzer. The EIS Nyquist plots were collected by applying the alternating current signal (10 mV) over the frequency range (100 kHz to 0.01 Hz) under AM 1.5G illumination at open-circuit conditions. To perform the Mott–Schottky analysis, the frequency was fixed at 1 kHz. The V_{oc} decay measurements were carried out by recording the V_{oc} value under AM 1.5G illumination, followed by monitoring subsequent decay after light irradiation was turned off. The Nernst equation, $E_{RHE} = E_{Ag/AgCl} + 0.059 \text{ pH} + E^0_{Ag/AgCl}$, was used to transform the measured potential (vs Ag/AgCl) to the potential against reversible hydrogen electrode (vs RHE). Here, E_{RHE} represents the converted potential versus RHE; $E_{Ag/AgCl}$ stands for the measured potential versus Ag/AgCl, and $E^0_{Ag/AgCl} = 0.199 \text{ V}$ (for saturated KCl) at 25 °C. The values of incident-photon-to-current-conversion-efficiency (IPCE) at specific wavelengths were determined from the equation $IPCE = (1240I)/(\lambda P_{light})$. Here, I denotes the photocurrent density, P_{light} stands for the incident power density, and λ represents the incident wavelength. The production of holes on the photoelectrode surface was estimated by

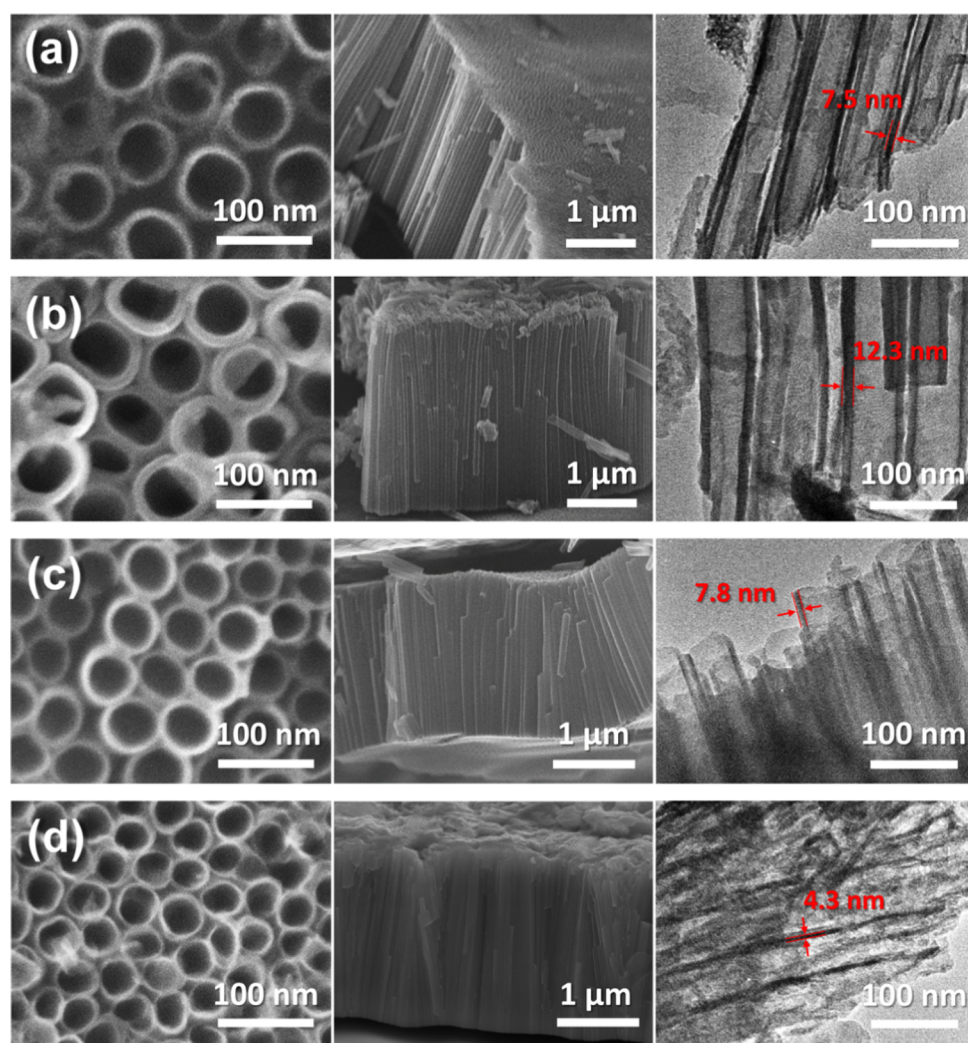


Figure 1. Top-view SEM, tilted-view SEM, and typical TEM images for (a) pristine TiO_2 , (b) TNTZO-1, (c) TNTZO-2, and (d) TNTZO-3 nanotube arrays.

using N,N,N',N' -tetramethyl-*p*-phenylenediamine (TMPD) as the chromogenic reagent.⁴² Note that TMPD can react with photo-generated holes to form its cationic radical form ($\text{TMPD}^{\bullet+}$), which can be characterized by measuring the absorption spectrum. To perform the measurement, an Ar-saturated acetonitrile solution (30 mL) in which a fixed amount of TMPD (120 mg) was dissolved was employed as the electrolyte. Upon light illumination for a certain period, the electrolyte solution was sampled and analyzed with an absorption spectroscope.

2.3. Characterizations. The morphology of the nanotube samples was examined on a scanning electron microscope (SEM, JEOL, JSM-6700F) and a scanning transmission electron microscope (STEM, JEOL, JEM-2100). The crystallinity and crystal structure were inspected on an X-ray diffractometer (XRD, Rigaku, RINT-2000). The chemical compositions were analyzed with the energy-dispersive X-ray spectroscope (EDS, an attachment to STEM) and X-ray photoelectron spectrometer (XPS, VG Scientific, Microlab 350). The C 1s peak at 284.6 eV was utilized to correct the recorded binding energies. The diffuse reflectance and absorption spectra were received from the spectrophotometer (Hitachi, U-3900H). The steady-state PL spectra were obtained on the fluorescence spectrometer (Kimmon IK3001R-G) using He–Cd laser (720 W) as the excitation source. To measure time-resolved PL spectra, a sub-nanosecond pulsed diode laser ($\lambda = 320$ nm, PicoQuant, PLD 320) installed on a customized single photon counting system was used. The signals recorded from the band-edge emission of the samples were analyzed with a biexponential decay model.

3. RESULTS AND DISCUSSION

The obtained nanotube arrays were first studied with SEM to observe the microstructure. Figure 1 displays the SEM images for the nanotubes anodically grown from the Ti foils and $\text{Ti}_{29}\text{Nb}_{13}\text{Ta}_{4.6}\text{Zr}$ alloys. Note that the anodization time was suitably tuned to achieve a comparable nanotube length for the different samples (approximately 2 μm), which eliminated the influence of nanotube length on the resultant PEC performance. For pristine TiO_2 from the Ti foils, the organized nanotubes were tightly packed with a wall thickness of 7.3 ± 0.8 nm and an inner diameter of 54.5 ± 4.2 nm. The grown TNTZO nanotubes were also highly ordered and stacked with each other. Notably, tuning the water content of electrolyte evinced the growth of TNTZO nanotube arrays with distinct geometric features, i.e., varied inner diameters and wall thicknesses. When the water content decreased from 20 to 10 vol %, the inner diameter of the TNTZO nanotubes decreased from 50.0 ± 4.0 to 45.2 ± 2.5 nm. As the water content was further reduced to 0.9 vol %, the inner diameter of TNTZO largely decreased to 33.6 ± 3.9 nm. Such a decrease in the nanotube size can be understood from the retarded fluoride ion diffusion at a relatively low water content condition, which suppressed chemical dissolution for the grown oxides.⁴³ The

wall thicknesses of the grown nanotubes decreased monotonically with decreasing water content. As the water content was reduced from 20, 10, to 0.9 vol %, the wall thickness of TNTZO decreased from 12.6 ± 1.0 (TNTZO-1) to 7.7 ± 0.8 (TNTZO-2) and then 3.5 ± 0.5 nm (TNTZO-3). Such an observation was in line with literature reports on the anodization of Ti, in which the nanotube wall thickness of the grown TiO_2 decreased with decreasing water content in the electrolyte.^{44,45} Importantly, a reduction in the wall thickness to less than 5 nm has significant implications for advancing the PEC properties of semiconductor nanotubes because the kinetics of hole transportation from semiconductor to electrolyte can be facilitated under such a confined size regime,^{16,18} which will be demonstrated later in the charge dynamics measurements. The structural porosity was further determined to better describe the distinct geometric features for the present TNTZO nanotube arrays,¹⁶ which was 49.4, 59.7, and 71.5% for TNTZO-1, TNTZO-2, and TNTZO-3, respectively.

To examine the composition of the samples, we subsequently performed XRD, STEM-EDS, and XPS analyses. In Figure 2a,

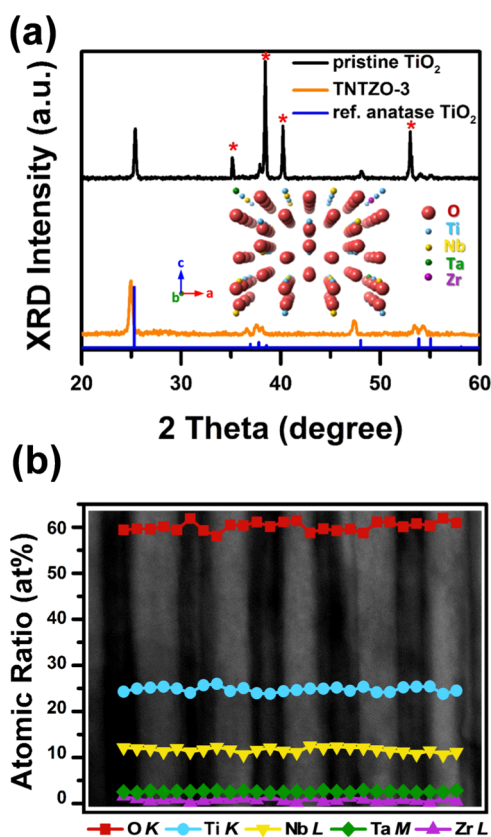


Figure 2. (a) XRD patterns for pristine TiO_2 and TNTZO nanotubes. The inserted marks (*) represent the signals of the Ti foil, and the inset shows the schematic crystal structure of TNTZO. (b) STEM-EDS line-scan analysis taken on the lateral side of TNTZO nanotube arrays.

the XRD patterns characterized both pristine TiO_2 and TNTZO nanotubes as the regular anatase phase of TiO_2 . For the TNTZO, there were no diffraction peaks attributable to Nb oxide, Ta oxide, Zr oxide, or other impurities, suggesting that the Nb, Ta, and Zr elements were homogeneously mixed with TiO_2 instead of forming a secondary phase. Besides, the three TNTZO samples exhibited diffraction patterns with the peak

intensity ratios quite close to those of pristine TiO_2 , reflecting that pristine TiO_2 and TNTZO nanotubes grown from the current electrochemical anodization process shared identical crystallographic orientations. Compared with pristine TiO_2 , the (101) diffraction peak of TNTZO, however, slightly shifted to a lower 2θ value, pointing out an increase in the interlayer spacing for TNTZO as a result of the substitutional replacement of Ti^{4+} with Nb^{5+} , Ta^{5+} , and Zr^{4+} , which have larger atomic sizes.^{39,46,47} In Figure 2b, the STEM-EDS line-scan analysis taken across several compacted nanotubes of TNTZO further reveals the uniformity of the elemental compositions. This outcome correlated to the result of XRD characterization, which reflects a homogeneous distribution of Ti, Nb, Ta, and Zr within the TNTZO lattice. According to the EDS result, the content of Ti, Nb, Ta, and Zr was, respectively, determined to be 24.79, 11.65, 2.59, and 0.78 at. %, similar to the composition of the starting $\text{Ti}_{29}\text{Nb}_{13}\text{Ta}_{4.6}\text{Zr}$ alloy. To receive insights into the chemical states of the constituent elements, XPS measurements were further conducted. As Figure 3 shows, pristine TiO_2 presented a typical Ti 2p spectrum, with binding energies matching the reported values.⁴⁸ For the three TNTZO nanotubes, the core-level profiles of Nb 3d, Ta 4f, and Zr 3d displayed binding energies associated with the Nb^{5+} , Ta^{5+} , and Zr^{4+} oxidation states. However, the Ti 2p spectra of TNTZO exhibited a positive binding energy shift relative to pristine TiO_2 . The prevalence of electronic interaction between TiO_2 and the introduced Nb, Ta, and Zr elements may account for such chemical shifts.

The absorption and PL spectroscopy were utilized to investigate the optical behaviors. As Figure 4a presents, an eminent light absorption onset at around 370 nm was noticed for both pristine TiO_2 and TNTZO, which was ascribed to the excitonic absorption of the constituent TiO_2 . The Tauc plot of Figure 4b determines the apparent bandgap values of 3.38, 3.31, 3.27, and 3.25 eV for pristine TiO_2 , TNTZO-1, TNTZO-2, and TNTZO-3, respectively. The relatively smaller bandgap of the three TNTZO possibly originates from the introduced Nb, Ta, and Zr elements, which may have evoked interband transitions within the energy gap of TiO_2 and reduced the apparent bandgap. More importantly, the observed pronounced light absorption for the TNTZO nanotubes suggests the capability of effective photon harvesting for solar conversion. Figure 4c presents the steady-state PL spectra of pristine TiO_2 and the three TNTZO nanotubes. All of the samples exhibited a broad emission band from 350 to 750 nm, which consisted of a band-edge emission at about 380 nm and a trap-state emission centered around 530 nm.⁴⁹ For n-type oxide semiconductors (e.g., ZnO and TiO_2), oxygen vacancies are regarded as the most probable trap states that can capture charge carriers to induce visible emission.^{49,50} As compared to pristine TiO_2 , the three TNTZO nanotubes showed considerably depressed trap-state emission, suggesting the reduced amount of oxygen vacancies for TNTZO. Because Nb and Ta have a higher valence state than Ti, their incorporation into TiO_2 can suppress the formation of oxygen vacancies owing to the electroneutrality,³⁹ which may account for the depressed trap-state emission of TNTZO. Note that the PEC performance of TNTZO can benefit from the removal of trap states because charge carrier transfer can be facilitated. Time-resolved PL data were further collected and studied to acquire the charge dynamics information in terms of the exciton lifetime, which offers a direct indicator for evaluating the PEC performance of

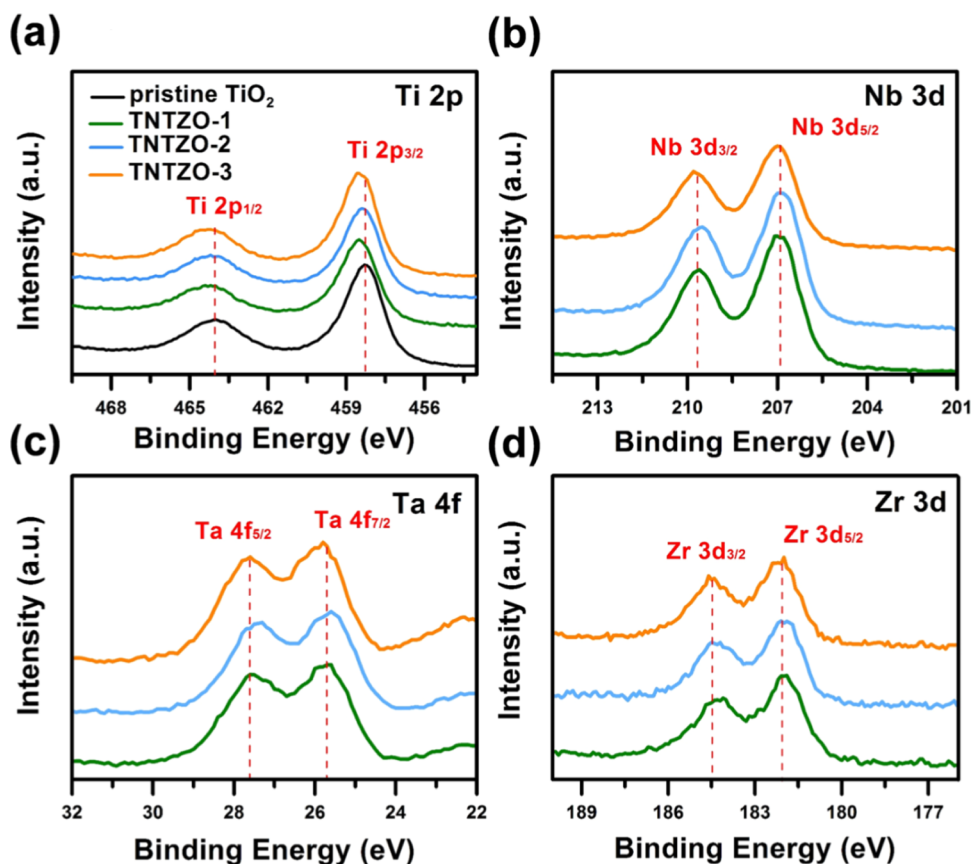


Figure 3. XPS spectra of (a) Ti 2p, (b) Nb 3d, (c) Ta 4f, and (d) Zr 3d core levels for pristine TiO_2 and the three TNTZO nanotubes.

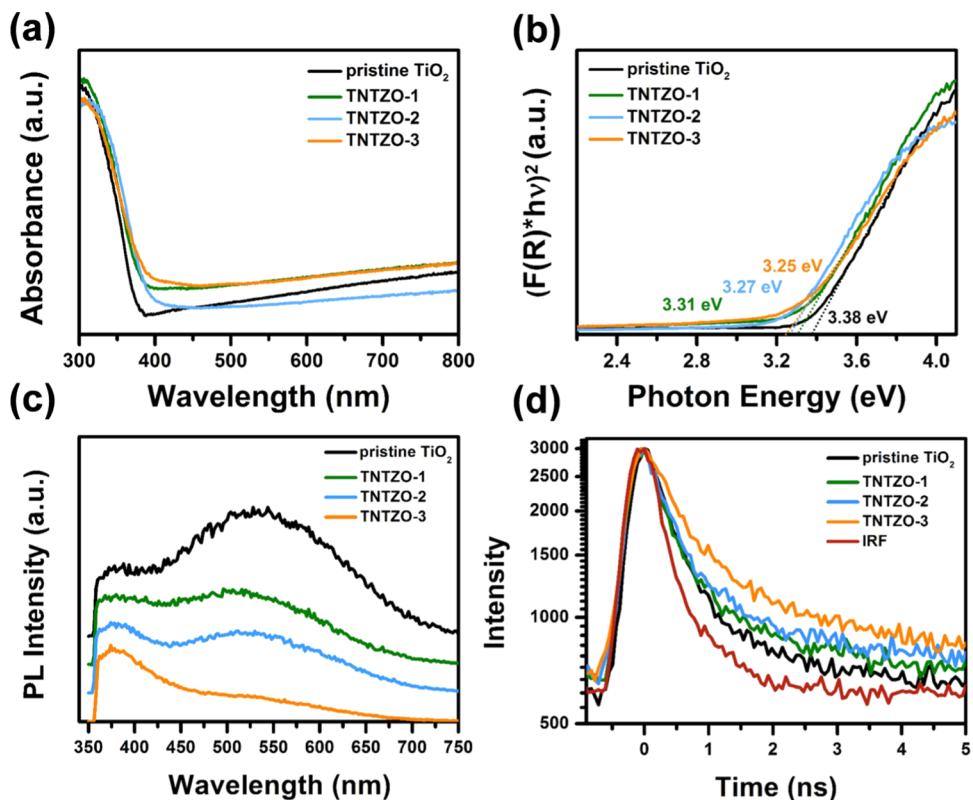


Figure 4. (a) Diffuse reflectance spectra, (b) the resultant Tauc plots, (c) steady-state PL spectra, and (d) time-resolved PL spectra for pristine TiO_2 and the three TNTZO nanotubes.

the samples.^{51,52} The long exciton lifetime signifies the lasting exciton survival, thereby enabling further carrier participation in the PEC reactions. Figure 4d displays the time-resolved PL spectra for the four relevant samples. In comparison with pristine TiO₂, the three TNTZO nanotubes exhibited deferred PL decay kinetics, indicating the long-lived characteristics for the excitons in TNTZO. These spectra were then fitted with a biexponential decay model to generate an intensity-weighted exciton lifetime ($\langle\tau\rangle$). As itemized in Table 1, the three

Table 1. Fitted Kinetics Parameters of the Time-Resolved PL Data for Pristine TiO₂ and the Three TNTZO

entry	A ₁ (%)	τ ₁ (ns)	A ₂ (%)	τ ₂ (ns)	⟨τ⟩ (ns)	χ ²
pristine TiO ₂	1.7	3.60	98.3	0.15	1.14	1.112
TNTZO-1	2.4	3.70	97.6	0.15	1.49	1.238
TNTZO-2	2.7	3.75	97.3	0.16	1.56	1.143
TNTZO-3	5.9	3.83	94.1	0.23	2.08	1.130

TNTZO nanotubes showed longer exciton lifetime than that of pristine TiO₂, with the TNTZO-3 having the longest value of 2.08 ns. As the steady-state PL spectra demonstrated, the amount of trap states was largely reduced in TNTZO, which may suppress the nonradiative recombination of charge carriers and thus extend the exciton lifetime.

The essentially long exciton lifetime and one-dimensional geometric features give the present TNTZO nanotube arrays a virtually promising position for applications in PEC processes. In particular, the substantially thin wall thickness and considerably high nanotube porosity of TNTZO-3 may facilitate hole-transfer kinetics¹⁸ and accelerate molecular migration in the tube,¹⁶ both of which are favorable for promoting PEC water splitting. To examine the practice in PEC cells, the TNTZO was employed as the photoanode to perform electrolytic water splitting. Figure 5a shows the typical *I*-*V* curves for pristine TiO₂ and TNTZO electrodes, which displayed several important features. First, the dark scans exhibited a fairly low current density (approximately 10⁻⁷ A cm⁻²), revealing that both TiO₂ and TNTZO were considerably stable during their operation in an alkaline electrolyte. Second, compared with pristine TiO₂, the three TNTZO electrodes displayed higher saturated photocurrent densities, disclosing the intriguing photoactive nature of TNTZO. Here, we attributed the enhanced photoactivity of

TNTZO to the introduced Nb, Zr, and Ta elements, which not only induced shallow donor states to increase the carrier concentration, but also suppressed trap states formation to facilitate charge carrier transfer.³⁵⁻³⁹ The above supposition will be later validated with EIS and *V*_{oc} decay analysis. Third, among the three TNTZO electrodes tested, TNTZO-3 attained the highest photocurrent generation of 0.28 mA cm⁻² at 0 V versus Ag/AgCl (+1.02 V vs RHE). In practice, nanotube arrays possessing a wall thickness substantially smaller than the hole diffusion length (around 10 nm for TiO₂^{17,18}) are highly desired for the design of sophisticated photoanodes because the possible hole loss along the radial direction can be minimized. On the other hand, the large structural porosity may equip the nanotube arrays with abundant inner space for accelerating molecular migration inside the tube, which also helps to enhance the kinetics of water oxidation reaction.¹⁶ Because the geometric feature of TNTZO-3 was characteristic of the thinnest wall thickness (3.5 nm) and the largest structural porosity (71.5%), the resultant PEC performance was predominant over TNTZO-1 and TNTZO-2. To investigate the instant photoresponse behavior, the *I*-*t* curves were measured under chopped light irradiation. As Figure 5b shows, the photocurrent generation of TNTZO quickly reached a steady state without any accompanying spikes; under the light-off condition, the photocurrents were quickly reduced to nearly zero without exhibiting a photocurrent tail. This phenomenon signified that the photocurrent generation of TNTZO was instantaneous without the occurrence of carrier trapping events,^{53,54} which is an important merit for consideration as a practical photoelectrode.

Assuming Faradaic efficiency of 100%, the efficiency of converting photon energy to chemical energy can be quantitatively determined, offering a direct index to estimate the intrinsic performance of semiconductor photoelectrodes. By using the *I*-*V* data, the photoconversion efficiency (η) of the electrodes can be estimated from the expression: $\eta = [I \times (1.23 - |V_{\text{bias}}|)] / P_{\text{light}}$ ^{26,27} where *I* is the photocurrent density at the measured potential, *P*_{light} is the incident power density (100 mW cm⁻²), and *V*_{bias} is the applied potential. It is important to remark that *V*_{bias} stands for an actual potential applied to the working electrode. For a three-electrode cell, as configured in the present work, the potential value measured at the working electrode was simply apparent, which should be corrected with the corresponding open-circuit potential to

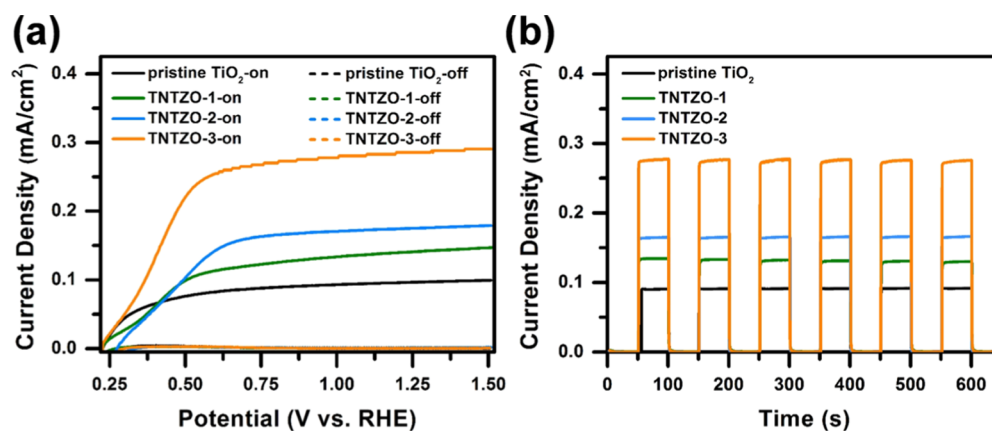


Figure 5. (a) *I*-*V* curves of pristine TiO₂ and the three TNTZO electrodes recorded under darkness and AM 1.5G illumination. (b) The corresponding *I*-*t* curves obtained at 0 V vs Ag/AgCl (+1.02 V vs RHE) under chopped light irradiation.

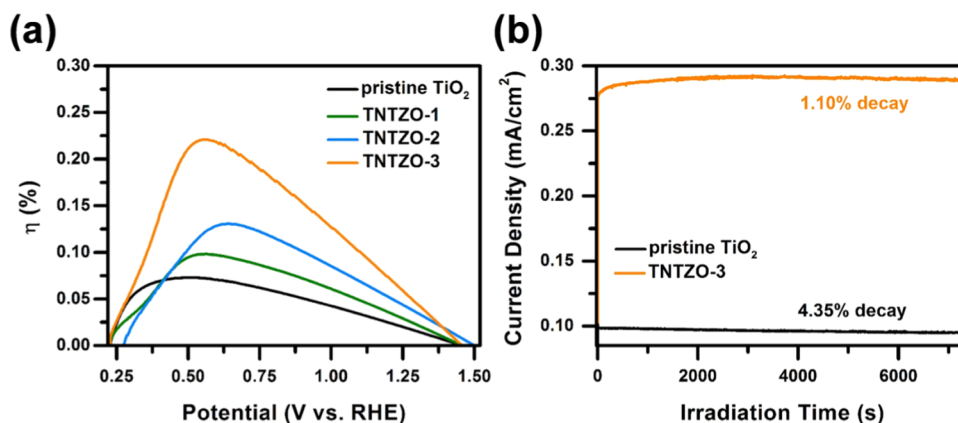


Figure 6. (a) Photoconversion efficiency (η) vs applied potential curves for pristine TiO_2 and the three TNTZO electrodes. (b) Photocurrent vs time data of pristine TiO_2 and TNTZO-3 recorded at 0 V vs Ag/AgCl (+1.02 V vs RHE).

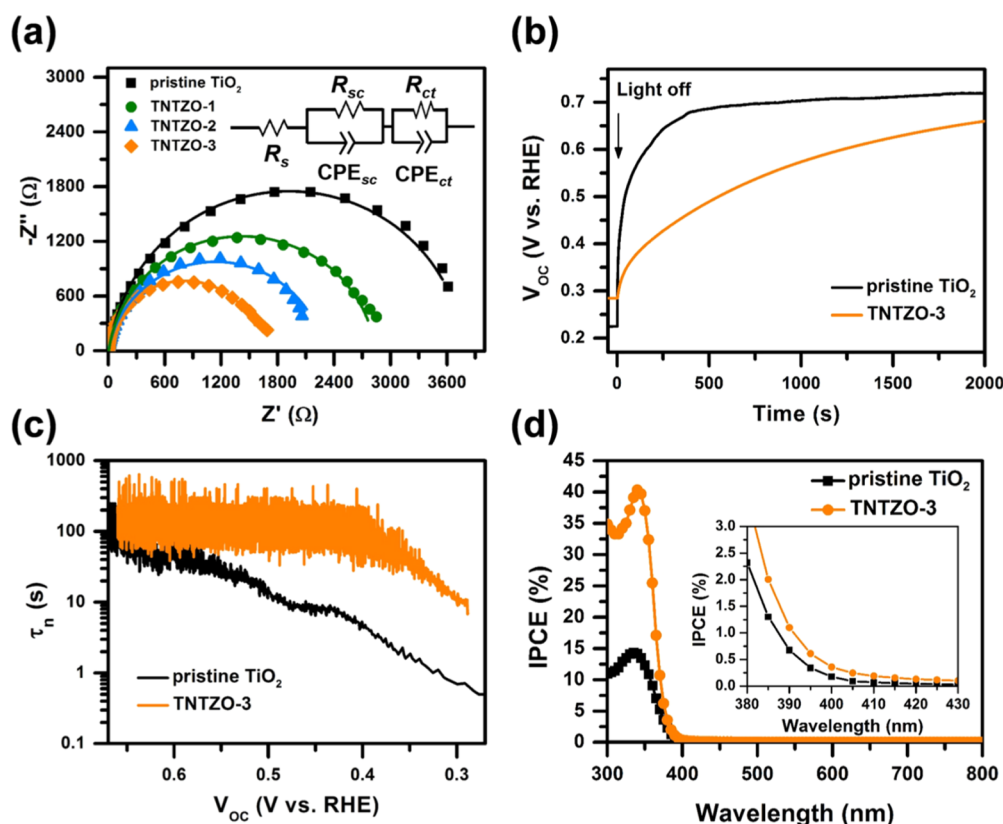


Figure 7. (a) Nyquist plots measured from pristine TiO_2 and the three TNTZO electrodes. An equivalent circuit used for data fitting is inserted, and the fitting data are plotted with solid curves. (b) Response of V_{oc} after the removal of light irradiation for pristine TiO_2 and TNTZO-3. (c) Calculated τ_n as a function of V_{oc} for pristine TiO_2 and TNTZO-3. (d) IPCE spectra for pristine TiO_2 and TNTZO-3 recorded at 0 V vs Ag/AgCl (+1.02 V vs RHE).

receive the empirical V_{bias} . Here, V_{bias} can be determined by $V_{bias} = V_{mea} - V_{voc}$, where V_{mea} stands for the potential of working electrode (vs RHE) where the photocurrent is measured and V_{voc} denotes the potential of the same working electrode (vs RHE) measured under the same irradiation at open-circuit conditions. As Figure 6a shows, under AM 1.5G illumination, the obtained maximum η of TNTZO-3 was approximately 0.22%, much higher than the values on pristine TiO_2 (0.07%), TNTZO-1 (0.10%), and TNTZO-2 (0.13%). Note that this value was comparable to those achieved from the sophisticated doped TiO_2 photoanodes, such as Ti^{3+} self-doped TiO_2 ,⁵⁵ Co-doped TiO_2 ,²⁷ Fe-doped TiO_2 ,⁵⁶ F-doped TiO_2 ,²⁵

and Ni-doped TiO_2 ,^{57,58} illustrating that the present TNTZO can function as a competent photoelectrode platform for various PEC reactions. It is also important to mention that the photoconversion efficiency defined by $\eta = [I \times (1.23 - |V_{bias}|)] / P_{light}$ merely serves as a diagnostic measure on the individual photoelectrode, not the overall cell performance. Nevertheless, the independent estimate on photoanodes or photocathodes may provide insightful information regarding the optimization of the integrated PEC systems capable of practical solar fuel production.^{59,60} Another important criterion for a reliable photoelectrode lies in the steady, sustainable photocurrent generation. To assess the durability, we recorded

Table 2. Fitted Parameters of the Nyquist Plots for Pristine TiO₂ and the Three TNTZO

entry	R _s (Ω)	R _{sc} (Ω)	CPEsc ^a		R _{ct} (Ω)	CPEct ^a	
			Q (mFs ⁿ⁻¹)	n		Q (mFs ⁿ⁻¹)	n
pristine TiO ₂	3.15	392.60	1.76	0.76	3382.0	0.33	0.98
TNTZO-1	4.56	1.56	0.39	0.63	2840.0	0.16	0.93
TNTZO-2	1.71	0.37	3.28	0.67	2278.0	0.80	0.91
TNTZO-3	1.82	0.11	3.16	0.88	1618.0	1.06	0.97

^aCPE is the constant phase element, and its impedance is given by $Z_{CPE} = Q^{-1}(j\omega)^{-n}$, in which Q denotes the pseudocapacitance, ω symbolizes the angular frequency, n stands for the CPE exponent ($0 \leq n \leq 1$), and j is the imaginary number.

the photocurrent density of TNTZO in the PEC cell over a long period of time. As Figure 6b illustrates, the photocurrent generation of TNTZO-3 was as stable as that of pristine TiO₂, which only dropped 1.10% upon continuous illumination for 2 h. This demonstration reveals the excellent chemical and structural stability for the TNTZO during operation in the PEC cell.

To validate the supposition regarding the cause of the enhanced photoactivity for TNTZO, we further carried out EIS analysis to comprehend the charge-transfer processes at the interface. Figure 7a displays the characteristic Nyquist plots in which well-defined semicircular curves were present. The diameter of the semicircular curves reflects the charge-transfer resistance of the tested electrode, with the smaller diameter signifying more efficient charge transfer. Obviously, the three TNTZO electrodes showed a more compressed arc than that of pristine TiO₂, implying enhanced charge-transfer dynamics for TNTZO presumably due to suppressed trap-state formation. To interpret the Nyquist data, an appropriate equivalent circuit composed of two RC elements connected in series was further used for data fitting.²⁸ In this model, the resistive and capacitive elements were directly related to individual charge-transfer processes associated with the oxidation of water. As depicted in Figure 7a, R_s is the overall series resistance of the circuit, which contains the sheet resistance of the substrate and the external contact resistance of PEC cell, R_{sc} is the charge-transfer resistance inside the semiconductor electrode, and R_{ct} corresponds to the charge-transfer resistance at the semiconductor/electrolyte interface. Furthermore, to better describe the nonideal capacitance behavior for the nanostructured samples with rough surfaces, constant phase elements (CPEs) were employed. Here, the R_{ct} component defines the process of hole transportation from the electrode surface to electrolyte. Significantly, R_{ct} represents a direct index for assessing the most decisive factor affecting the overall PEC performance. As Table 2 summarizes, the three TNTZO electrodes all exhibited an R_{ct} value much smaller than the value of pristine TiO₂, with the TNTZO-3 showing the lowest R_{ct}. This R_{ct} variation trend was fundamentally consistent with the results of PEC data and time-resolved PL analysis, corroborating that the enhanced photoactivity of TNTZO arose from the improved charge-transfer dynamics rendered by the trap-state depression. To acquire a more in-depth understanding on the charge-transfer and recombination behaviors, the time-dependent decay of V_{oc} upon the cease of illumination was monitored and analyzed. In this experiment, the photoexcited electrons were first accumulated in the photoelectrode at open-circuit conditions to cause an increase in the V_{oc}. Once the light was switched off, the accumulated electrons were recombined with the trapped holes or captured by the trap states,⁶¹ gradually reducing the V_{oc} with a decay rate related to the lifetime of the photoexcited electrons. Figure 7b plots the V_{oc} decay profiles recorded upon

the removal of irradiation for the two representative electrodes, pristine TiO₂ and TNTZO-3. Evidently, the TNTZO-3 electrode showed a slower V_{oc} decay rate than that of pristine TiO₂, indicating suppression of nonradiative charge recombination within the TNTZO. Using the equation $\tau_n = -\left(\frac{k_B T}{e_0}\right)\left(\frac{dV_{oc}}{dt}\right)^{-1}$,²⁴ where k_B is the Boltzmann constant ($k_B = 1.38 \times 10^{-23} \text{ m}^2 \text{ kg s}^{-2} \text{ K}^{-1}$), e_0 is the electron charge ($e_0 = 1.60 \times 10^{-19} \text{ C}$), and T is the temperature, the photoexcited electron lifetime (τ_n), which represents the average time for the photoexcited electrons to survive before dissipation, can be calculated. Figure 7c compares the calculated τ_n as a function of V_{oc} for the two electrodes. At the same V_{oc} value, the τ_n of the TNTZO-3 electrode was much longer than that of pristine TiO₂, reaffirming that the amount of trap states was largely reduced in TNTZO, which suppressed nonradiative charge recombination to prolong the lifetime of photoexcited electrons. To correlate the photoactivity with the absorption spectra, the IPCE data were collected by recording the photocurrent generation at different incident wavelengths. Figure 7d shows the IPCE spectra for pristine TiO₂ and TNTZO-3 electrodes. As compared to pristine TiO₂, the TNTZO-3 exhibited much enhanced IPCE across the bandgap absorption region, consistent with the results of PEC measurements. Importantly, the two electrodes displayed PEC activities spectrally matching with the corresponding absorption spectra, with the TNTZO-3 showing rather extended IPCE onset as a result of the reduced bandgap.

On the other hand, we conducted Mott–Schottky analysis to estimate the concentration of charge carriers available for PEC reactions. In Figure 8a, the linear fit to the Mott–Schottky plot has a positive slope, signifying that both pristine TiO₂ and TNTZO were n-type, as expected. The concentration of charge carriers can be estimated from the Mott–Schottky equation $\frac{1}{C^2} = \left(\frac{2}{e_0 \epsilon \epsilon_0 N_d}\right)\left(V - V_{FB} - \frac{k_B T}{e_0}\right)$, where C is the capacitance, e_0 is the electron charge ($e_0 = 1.60 \times 10^{-19} \text{ C}$), ϵ is the dielectric constant ($\epsilon = 48$ for anatase TiO₂),⁶² ϵ_0 is the vacuum permittivity ($\epsilon_0 = 8.85 \times 10^{-14} \text{ F cm}^{-1}$), N_d is the carrier density, V_{FB} is the flat-band potential, k_B is the Boltzmann constant ($k_B = 1.38 \times 10^{-23} \text{ m}^2 \text{ kg s}^{-2} \text{ K}^{-1}$), and T is the temperature. The N_d value can then be computed by using the slope of the $1/C^2$ versus V plot in Figure 7a, which was 1.73×10^{19} , 7.28×10^{19} , 1.17×10^{20} , and $1.27 \times 10^{20} \text{ cm}^{-3}$ for pristine TiO₂, TNTZO-1, TNTZO-2, and TNTZO-3, respectively. The observed enlarged N_d for TNTZO unambiguously supports the argument that the introduction of Nb, Ta, and Zr elements increased the carrier concentration by inducing shallow donor states. At the expense of incremental carriers, the charge-transfer dynamics within the TNTZO can be enhanced. Moreover, the depletion layer thickness (W_D) of the photoelectrodes, which is another decisive factor affecting the

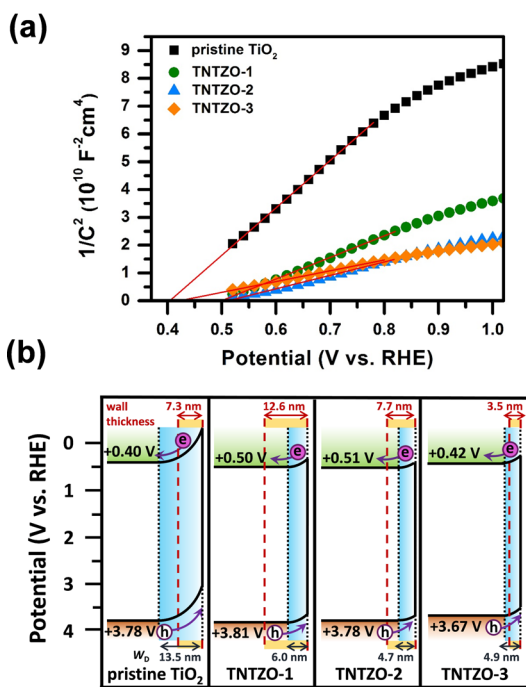


Figure 8. (a) Mott–Schottky plots measured from pristine TiO_2 and the three TNTZO electrodes. (b) Plausible electronic band structure for pristine TiO_2 and the three TNTZO electrodes.

outcome of the PEC performance, can also be acquired from the equation $W_D = \left[\frac{2e\epsilon_0(V - V_{FB})}{e_0 N_d} \right]^{1/2}$.⁶³ The Mott–Schottky equation suggests that when extrapolating $1/C^2$ to zero in Figure 8a, the intercept at the x axis gives a quantity $\left(V_{FB} + \frac{k_B T}{e_0} \right)$, which is used to determine the V_{FB} . In this regard, the Fermi level equals the measured V_{FB} because band bending vanished at flat-band conditions.⁶⁴ The results of the extrapolation operation gave rise to a Fermi level of around +0.40 V versus RHE for pristine TiO_2 , which agrees with the previously reported value.^{65,66} Compared with pristine TiO_2 , the three TNTZO nanotubes exhibited more positive Fermi levels ranging from +0.42 to +0.51 V versus RHE. Because the N_d values of pristine TiO_2 and TNTZO were considerably larger than the corresponding effective density of states ($2.51 \times 10^{19} \text{ cm}^{-3}$ for TiO_2 by using an electron effective mass of 1.0

m_e^{67}), the level of conduction band edge was suggested fairly close to the Fermi energy level,^{67,68} which was empirically equal to V_{FB} . By subtracting the apparent bandgap from the level of conduction band edge, it is practical to further obtain the level of valence band edge. Figure 8b depicts the plausible band structure for pristine TiO_2 and the three TNTZO nanotubes by using the calculated parameters. In Figure 8b, the values of W_D and nanotube wall thickness were also noted to highlight their implications. The calculated W_D at 0 V versus Ag/AgCl for pristine TiO_2 , TNTZO-1, TNTZO-2, and TNTZO-3 was 13.5, 6.0, 4.7, and 4.9 nm, respectively. Relative to pristine TiO_2 , the three TNTZO samples possessed much lower W_D values, which can largely shorten the time for photogenerated holes to transport from TNTZO to electrolyte and thereby facilitate the kinetics of water oxidation reaction.^{69,70} Special attention should be paid to the TNTZO-3 electrode, in which the nanotube wall thickness (3.5 nm) was virtually smaller than the W_D (4.9 nm), symbolizing a fully depleted state for the electrode.⁵³ In this regime, the photoexcited electrons and holes could be entirely separated with the aid of an electric field biased across the whole radial dimension. Being driven by the electric field, the photogenerated holes can swiftly drift and inject into the electrolyte to oxidize water, which accounted for the particularly notable PEC performance observed for TNTZO-3. On the other hand, pristine TiO_2 was also fully depleted with the W_D (13.5 nm) much larger than the wall thickness (7.3 nm). The intrinsically pronounced charge recombination however compromised the fully depleted state to show a mediocre carrier utilization efficiency, as observed. Much importantly, the fully depleted TNTZO-3 nanotube arrays may offer a feasible and universal platform for the loading of other semiconductors to construct a sophisticated photoelectrode paradigm, in which the photoexcited charge carriers can be entirely utilized for realizing practical solar-to-fuel conversion. The findings from the Mott–Schottky analysis, together with the results of PEC measurements, time-resolved PL spectra, EIS analysis, and V_{oc} decay dynamics conclude that the introduction of the Nd, Ta, and Zr elements in TNTZO enhanced the amount of accessible charge carriers, modified the electronic structure, and improved the hole-transfer kinetics, thus expediting water splitting and enhancing the overall PEC efficiency.

To demonstrate the realistic applications, the hydrogen evolution in the PEC cell by employing TNTZO-3 as the photoanode was further monitored. As shown in the inset of

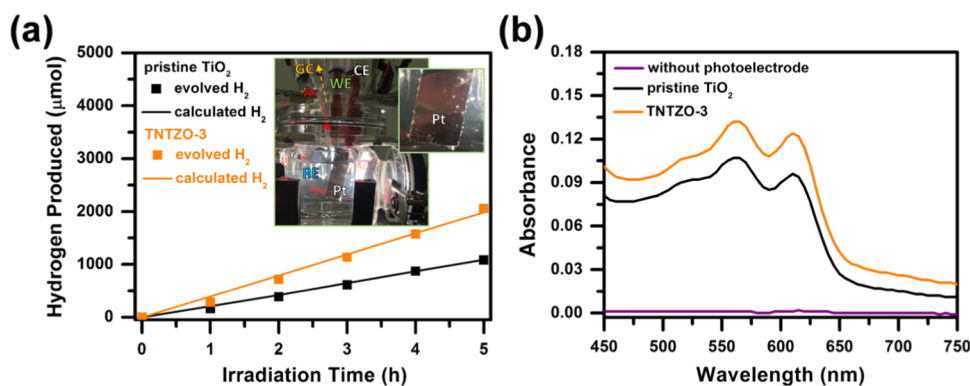


Figure 9. (a) Hydrogen evolution data for pristine TiO_2 and TNTZO-3 electrodes recorded in the PEC cell at 0 V vs Ag/AgCl (+1.02 V vs RHE). Insets show the cell configuration, in which WE, CE, RE, and Ar represent working, counter, and reference electrodes and argon purging, respectively. (b) UV–visible absorption spectra of TMPD solutions upon 45 min of light illumination over pristine TiO_2 and TNTZO-3 electrodes.

Figure 9a, abundant hydrogen bubbles evolved from the Pt counter electrode can be recognized with the naked eye. The hydrogen production rate obtained at TNTZO-3 was $411.2 \mu\text{mol h}^{-1}$, much higher than the $216.4 \mu\text{mol h}^{-1}$ from pristine TiO_2 . Significantly, the recorded hydrogen production rate was fairly close to the theoretical value calculated by assuming 100% of the Faradaic efficiency, verifying that the photocurrent generation from TNTZO indeed resulted from the PEC water splitting reaction. This illustration reveals that the fully depleted TNTZO-3 nanotubes can practically perform PEC water splitting to realize solar hydrogen production. To highlight the capacity of the photoelectrode for producing holes at the surface, we further examined the photo-oxidation reaction on the photoelectrode by employing TMPD as the chromogenic reagent.⁴² By directly reacting with holes, TMPD may undergo oxidation to generate a blue product ($\text{TMPD}^{\bullet+}$) that can be characterized by measuring the absorption spectrum. Figure 9b represents the formation of $\text{TMPD}^{\bullet+}$ over pristine TiO_2 and TNTZO-3 electrodes upon light illumination for a certain period. Evidently, TNTZO-3 performed better toward TMPD photo-oxidation than pristine TiO_2 did, which was conformable to the results of PEC measurements and hydrogen evolution.

4. CONCLUSIONS

By performing electrochemical anodization on $\text{Ti}_{29}\text{Nb}_{13}\text{Ta}_{4.6}\text{Zr}$ alloys, quaternary TNTZO mixed-oxide nanotube arrays with controllable geometric features were prepared. Compared with pristine TiO_2 , the TNTZO photoanodes exhibited noticeably enhanced photoactivity toward solar water splitting. The analytic results of time-resolved PL, EIS, and V_{oc} decay measurements manifest that the superior photoactivity of TNTZO originated from the introduction of Nd, Ta, and Zr elements, which enhanced the amount of accessible charge carriers, modified the electronic structure, and improved the hole-transfer kinetics for expediting water splitting. Furthermore, reducing the water content of the electrolyte to 0.9 vol % generated TNTZO-3 nanotubes that can be fully depleted during PEC operations, which may serve as a versatile structural backbone to construct a sophisticated photoelectrode paradigm. Unlike most of the past studies that only reported the PEC I - V and I - t data for the developed photoelectrodes, the present work examined the realistic hydrogen evolution by employing TNTZO as the photoanode in the PEC water splitting cell. This illustration reveals that the fully depleted TNTZO nanotubes can practically perform PEC water splitting to realize solar hydrogen production. Especially, with the nontoxic and biocompatible characteristics, the present TNTZO nanotube arrays may find virtually unique yet practically viable applications in biotechnologically important fields such as PEC biomolecule sensing and PEC biofuel reforming.

AUTHOR INFORMATION

Corresponding Authors

*E-mail: chen.c.ac@m.titech.ac.jp (C.-Y.C.).

*E-mail: chang.m.aa@m.titech.ac.jp (T.-F.M.C.).

*E-mail: yhsu@cc.nctu.edu.tw (Y.-J.H.).

ORCID

Yung-Jung Hsu: 0000-0003-3243-2644

Notes

The authors declare no competing financial interest.

ACKNOWLEDGMENTS

This work was financially supported by the Japan Science and Technology Agency (JST) with the CREST Project # 14531864, the Japan Society for the Promotion of Science (JSPS) with the Grant-in-Aid for Scientific Research KAKENHI # 26220907, and the Ministry of Science and Technology (MOST) of Taiwan under grants MOST 105-2119-M-009-003 and MOST 106-2113-M-009-025.

REFERENCES

- (1) Roy, P.; Kim, D.; Lee, K.; Spiecker, E.; Schmuki, P. TiO_2 nanotubes and their application in dye-sensitized solar cells. *Nanoscale* **2010**, *2*, 45–59.
- (2) Allam, N. K.; Grimes, C. A. Room Temperature One-Step Polyol Synthesis of Anatase TiO_2 Nanotube Arrays: Photoelectrochemical Properties. *Langmuir* **2009**, *25*, 7234–7240.
- (3) Liu, N.; Schneider, C.; Freitag, D.; Hartmann, M.; Venkatesan, U.; Müller, J.; Spiecker, E.; Schmuki, P. Black TiO_2 Nanotubes: Cocatalyst-Free Open-Circuit Hydrogen Generation. *Nano Lett.* **2014**, *14*, 3309–3313.
- (4) Xiao, F.-X.; Miao, J.; Wang, H.-Y.; Liu, B. Self-assembly of hierarchically ordered CdS quantum dots- TiO_2 nanotube array heterostructures as efficient visible light photocatalysts for photoredox applications. *J. Mater. Chem. A* **2013**, *1*, 12229–12238.
- (5) Sarkar, A.; Singh, A. K.; Sarkar, D.; Khan, G. G.; Mandal, K. Three-Dimensional Nanoarchitecture of BiFeO_3 Anchored TiO_2 Nanotube Arrays for Electrochemical Energy Storage and Solar Energy Conversion. *ACS Sustainable Chem. Eng.* **2015**, *3*, 2254–2263.
- (6) Zhang, H.; Liu, P.; Liu, X.; Zhang, S.; Yao, X.; An, T.; Amal, R.; Zhao, H. Fabrication of Highly Ordered TiO_2 Nanorod/Nanotube Adjacent Arrays for Photoelectrochemical Applications. *Langmuir* **2010**, *26*, 11226–11232.
- (7) Mohamed, A. M.; Aljaber, A. S.; AlQaradawi, S. Y.; Allam, N. K. TiO_2 nanotubes with ultrathin walls for enhanced water splitting. *Chem. Commun.* **2015**, *51*, 12617–12620.
- (8) Xiao, F.-X.; Hung, S.-F.; Miao, J.; Wang, H.-Y.; Yang, H.; Liu, B. Metal-Cluster-Decorated TiO_2 Nanotube Arrays: A Composite Heterostructure toward Versatile Photocatalytic and Photoelectrochemical Applications. *Small* **2015**, *11*, 554–567.
- (9) Li, Y.; Luo, S.; Wei, Z.; Meng, D.; Ding, M.; Liu, C. Electrodeposition technique-dependent photoelectrochemical and photocatalytic properties of an $\text{In}_2\text{S}_3/\text{TiO}_2$ nanotube array. *Phys. Chem. Chem. Phys.* **2014**, *16*, 4361–4368.
- (10) Altomare, M.; Lee, K.; Killian, M. S.; Selli, E.; Schmuki, P. Ta-Doped TiO_2 Nanotubes for Enhanced Solar-Light Photoelectrochemical Water Splitting. *Chem. – Eur. J.* **2013**, *19*, 5841–5844.
- (11) Das, C.; Roy, P.; Yang, M.; Jha, H.; Schmuki, P. Nb doped TiO_2 nanotubes for enhanced photoelectrochemical water-splitting. *Nanoscale* **2011**, *3*, 3094–3096.
- (12) Krbal, M.; Sopha, H.; Podzemna, V.; Das, S.; Prikryl, J.; Macak, J. M. TiO_2 Nanotube/Chalcogenide-Based Photoelectrochemical Cell: Nanotube Diameter Dependence Study. *J. Phys. Chem. C* **2017**, *121*, 6065–6071.
- (13) Gui, Q.; Xu, Z.; Zhang, H.; Cheng, C.; Zhu, X.; Yin, M.; Song, Y.; Lu, L.; Chen, X.; Li, D. Enhanced Photoelectrochemical Water Splitting Performance of Anodic TiO_2 Nanotube Arrays by Surface Passivation. *ACS Appl. Mater. Interfaces* **2014**, *6*, 17053–17058.
- (14) Fernandes, J. A.; Khan, S.; Baum, F.; Kohlrausch, E. C.; Santos, J. A. L. d.; Baptista, D. L.; Teixeira, S. R.; Dupont, J.; Santos, M. J. L. Synergizing nanocomposites of CdSe/ TiO_2 nanotubes for improved photoelectrochemical activity via thermal treatment. *Dalton Trans.* **2016**, *45*, 9925–9931.
- (15) Xiao, F.-X.; Miao, J.; Wang, H.-Y.; Yang, H.; Chen, J.; Liu, B. Electrochemical construction of hierarchically ordered CdSe-sensitized TiO_2 nanotube arrays: towards versatile photoelectrochemical water splitting and photoredox applications. *Nanoscale* **2014**, *6*, 6727–6737.
- (16) Liang, S.; He, J.; Sun, Z.; Liu, Q.; Jiang, Y.; Cheng, H.; He, B.; Xie, Z.; Wei, S. Improving Photoelectrochemical Water Splitting

Activity of TiO₂ Nanotube Arrays by Tuning Geometrical Parameters. *J. Phys. Chem. C* **2012**, *116*, 9049–9053.

(17) Cargnello, M.; Montini, T.; Smolin, S. Y.; Priebe, J. B.; Jaén, J. J. D.; Doan-Nguyen, V. V. T.; McKay, I. S.; Schwalbe, J. A.; Pohl, M.-M.; Gordon, T. R.; Lu, Y.; Baxter, J. B.; Brückner, A.; Fornasiero, P.; Murray, C. B. *Proc. Natl. Acad. Sci. U.S.A.* **2016**, *113*, 3966–3971.

(18) Mohamed, A. M.; Aljaber, A. S.; AlQaradawi, S. Y.; Allam, N. K. TiO₂ nanotubes with ultrathin walls for enhanced water splitting. *Chem. Commun.* **2015**, *51*, 12617–12620.

(19) Pu, Y.-C.; Wang, G.; Chang, K.-D.; Ling, Y.; Lin, Y.-K.; Fitzmorris, B. C.; Liu, C.-M.; Lu, X.; Tong, Y.; Zhang, J. Z.; Hsu, Y.-J.; Li, Y. Au Nanostructure-Decorated TiO₂ Nanowires Exhibiting Photoactivity Across Entire UV–visible Region for Photoelectrochemical Water Splitting. *Nano Lett.* **2013**, *13*, 3817–3823.

(20) Zhan, Z.; An, J.; Zhang, H.; Hansen, R. V.; Zheng, L. Three-Dimensional Plasmonic Photoanodes Based on Au-Embedded TiO₂ Structures for Enhanced Visible-Light Water Splitting. *ACS Appl. Mater. Interfaces* **2014**, *6*, 1139–1144.

(21) Liu, S.; Han, C.; Tang, Z.-R.; Xu, Y.-J. Heterostructured semiconductor nanowire arrays for artificial photosynthesis. *Mater. Horiz.* **2016**, *3*, 270–282.

(22) Ai, G.; Li, H.; Liu, S.; Mo, R.; Zhong, J. Solar Water Splitting by TiO₂/CdS/Co–Pi Nanowire Array Photoanode Enhanced with Co–Pi as Hole Transfer Relay and CdS as Light Absorber. *Adv. Funct. Mater.* **2015**, *25*, 5706–5713.

(23) Hensel, J.; Wang, G.; Li, Y.; Zhang, J. Z. Synergistic Effect of CdSe Quantum Dot Sensitization and Nitrogen Doping of TiO₂ Nanostructures for Photoelectrochemical Solar Hydrogen Generation. *Nano Lett.* **2010**, *10*, 478–483.

(24) Xiao, F.-X.; Miao, J.; Wang, H.-Y.; Yang, H.; Chen, J.; Liu, B. Electrochemical construction of hierarchically ordered CdSe-sensitized TiO₂ nanotube arrays: towards versatile photoelectrochemical water splitting and photoredox applications. *Nanoscale* **2014**, *6*, 6727–6737.

(25) Fang, W. Q.; Huo, Z.; Liu, P.; Wang, X. L.; Zhang, M.; Jia, Y.; Zhang, H.; Zhao, H.; Yang, H. G.; Yao, X. Fluorine-Doped Porous Single-Crystal Rutile TiO₂ Nanorods for Enhancing Photoelectrochemical Water Splitting. *Chem. – Eur. J.* **2014**, *20*, 11439–11444.

(26) Wang, G.; Wang, H.; Ling, Y.; Tang, Y.; Yang, X.; Fitzmorris, R. C.; Wang, C.; Zhang, J. Z.; Li, Y. Hydrogen-Treated TiO₂ Nanowire Arrays for Photoelectrochemical Water Splitting. *Nano Lett.* **2011**, *11*, 3026–3033.

(27) Wang, C.; Chen, Z.; Jin, H.; Cao, C.; Lia, J.; Mi, Z. Enhancing visible-light photoelectrochemical water splitting through transition-metal doped TiO₂ nanorod arrays. *J. Mater. Chem. A* **2014**, *2*, 17820–17827.

(28) Choi, M.; Lee, J. H.; Jang, Y. J.; Kim, D.; Lee, J. S.; Jang, H. M.; Yong, K. Hydrogen-doped Brookite TiO₂ Nanobullets Array as a Novel Photoanode for Efficient Solar Water Splitting. *Sci. Rep.* **2016**, *6*, No. 36099.

(29) Wang, G.; Xiao, X.; Li, W.; Lin, Z.; Zhao, Z.; Chen, C.; Wang, C.; Li, Y.; Huang, X.; Miao, L.; Jiang, C.; Huang, Y.; Duan, X. Significantly Enhanced Visible Light Photoelectrochemical Activity in TiO₂ Nanowire Arrays by Nitrogen Implantation. *Nano Lett.* **2015**, *15*, 4692–4698.

(30) Mor, G. K.; Prakasam, H. E.; Varghese, O. K.; Shankar, K.; Grimes, C. A. Vertically Oriented Ti–Fe–O Nanotube Array Films: Toward a Useful Material Architecture for Solar Spectrum Water Photoelectrolysis. *Nano Lett.* **2007**, *7*, 2356–2364.

(31) Mor, G. K.; Varghese, O. K.; Wilke, R. H. T.; Sharma, S.; Shankar, K.; Latempa, T. J.; Choi, K.-S.; Grimes, C. A. p-Type Cu–Ti–O Nanotube Arrays and Their Use in Self-Biased Heterojunction Photoelectrochemical Diodes for Hydrogen Generation. *Nano Lett.* **2008**, *8*, 1906–1911.

(32) Allam, N. K.; Alamgir, F.; El-Sayed, M. A. Enhanced Photoassisted Water Electrolysis Using Vertically Oriented Anodically Fabricated Ti–Nb–Zr–O Mixed Oxide Nanotube Arrays. *ACS Nano* **2010**, *4*, 5819–5826.

(33) Fukuda, A.; Takemoto, M.; Saito, T.; Fujibayashi, S.; Neo, M.; Yamaguchi, S.; Kizuki, T.; Matsushita, T.; Niinomi, M.; Kokubo, T.;

Nakamura, T. Bone bonding bioactivity of Ti metal and Ti–Zr–Nb–Ta alloys with Ca ions incorporated on their surfaces by simple chemical and heat treatments. *Acta Biomater.* **2011**, *7*, 1379–1386.

(34) Bărbînță, A. C.; Mareci, D.; Chelariu, R.; Bolat, G.; Munteanu, C.; Cho, K.; Niinomi, M. The estimation of corrosion behavior of new TiNbTaZr alloys for biomedical applications. *Mater. Corros.* **2014**, *65*, 1017–1023.

(35) Yang, M.; Jha, H.; Liu, N.; Schmuki, P. Increased photocurrent response in Nb-doped TiO₂ nanotubes. *J. Mater. Chem.* **2011**, *21*, 15205–15208.

(36) Yang, M.; Kim, D.; Jha, H.; Lee, K.; Paul, J.; Schmuki, P. Nb doping of TiO₂ nanotubes for an enhanced efficiency of dye-sensitized solar cells. *Chem. Commun.* **2011**, *47*, 2032–2034.

(37) Mohamed, I. M. A.; Dao, V.-D.; Barakat, N. A. M.; Yasin, A. S.; Yousef, A.; Choi, H.-S. Efficiency enhancement of dye-sensitized solar cells by use of ZrO₂-doped TiO₂ nanofibers photoanode. *J. Colloid Interface Sci.* **2016**, *476*, 9–19.

(38) Singh, N.; Prakash, J.; Misra, M.; Sharma, A.; Gupta, R. K. Dual Functional Ta-Doped Electrospun TiO₂ Nanofibers with Enhanced Photocatalysis and SERS Detection for Organic Compounds. *ACS Appl. Mater. Interfaces* **2017**, *9*, 28495–28507.

(39) Nakada, A.; Nishioka, S.; Vequizo, J. J. M.; Muraoka, K.; Kanazawa, T.; Yamakata, A.; Nozawa, S.; Kumagai, H.; Adachi, S.-i.; Ishitania, O.; Maeda, K. Solar-driven Z-scheme water splitting using tantalum/nitrogen co-doped rutile titania nanorod as an oxygen evolution photocatalyst. *J. Mater. Chem. A* **2017**, *5*, 11710–11719.

(40) Chiu, Y.-H.; Chang, K.-D.; Hsu, Y.-J. Plasmon-mediated charge dynamics and photoactivity enhancement for Au-decorated ZnO nanocrystals. *J. Mater. Chem. A* **2018**, *6*, 4286–4296.

(41) Chang, Y.-S.; Choi, M.; Baek, M.; Hsieh, P.-Y.; Yong, K.; Hsu, Y.-J. CdS/CdSe co-sensitized brookite H:TiO₂ nanostructures: Charge carrier dynamics and photoelectrochemical hydrogen generation. *Appl. Catal., B* **2018**, *225*, 379–385.

(42) Ma, B. C.; Ghasimi, S.; Landfester, K.; Vilela, F.; Zhang, K. A. I. Conjugated microporous polymer nanoparticles with enhanced dispersibility and water compatibility for photocatalytic applications. *J. Mater. Chem. A* **2015**, *3*, 16064–16071.

(43) Yin, H.; Liu, H.; Shen, W. Z. The large diameter and fast growth of self-organized TiO₂ nanotube arrays achieved via electrochemical anodization. *Nanotechnology* **2010**, *21*, No. 035601.

(44) Albu, S. P.; Roy, P.; Virtanen, S.; Schmuki, P. Self-organized TiO₂ Nanotube Arrays: Critical Effects on Morphology and Growth. *Isr. J. Chem.* **2010**, *50*, 453–467.

(45) Ozkan, S.; Nguyen, N. T.; Mazare, A.; Cerri, I.; Schmuki, P. Controlled spacing of self-organized anodic TiO₂ nanotubes. *Electrochem. Commun.* **2016**, *69*, 76–79.

(46) Wang, J.; Yu, Y.; Li, S.; Guo, L.; Wang, E.; Cao, Y. Doping Behavior of Zr⁴⁺ Ions in Zr⁴⁺-Doped TiO₂ Nanoparticles. *J. Phys. Chem. C* **2013**, *117*, 27120–27126.

(47) Jung, S.-Y.; Ha, T.-J.; Seo, W.-S.; Lim, Y. S.; Shin, S.; Cho, H. H.; Park, H.-H. Thermoelectric Properties of Nb-Doped Ordered Mesoporous TiO₂. *J. Electron. Mater.* **2011**, *40*, 652–656.

(48) Ni, J.; Fu, S.; Wu, C.; Maier, J.; Yu, Y.; Li, L. Self-Supported Nanotube Arrays of Sulfur-Doped TiO₂ Enabling Ultrastable and Robust Sodium Storage. *Adv. Mater.* **2016**, *28*, 2259–2265.

(49) Wang, X.; Feng, Z.; Shi, J.; Jia, G.; Shen, S.; Zhou, J.; Li, C. Trap states and carrier dynamics of TiO₂ studied by photoluminescence spectroscopy under weak excitation condition. *Phys. Chem. Chem. Phys.* **2010**, *12*, 7083–7090.

(50) Kavitha, M. K.; Jinesh, K. B.; Philip, R.; Gopinath, P.; John, H. Defect engineering in ZnO nanocones for visible photoconductivity and nonlinear absorption. *Phys. Chem. Chem. Phys.* **2014**, *16*, 25093–25100.

(51) Lin, W.-H.; Chang, T.-F. M.; Lu, Y.-H.; Sato, T.; Sone, M.; Wei, K.-H.; Hsu, Y.-J. Supercritical CO₂-Assisted Electrochemical Deposition of ZnO Mesocrystals for Practical Photoelectrochemical Applications. *J. Phys. Chem. C* **2013**, *117*, 25596–25603.

(52) Chen, Y.-C.; Liu, T.-C.; Hsu, Y.-J. ZnSe-0.5N₂H₄ Hybrid Nanostructures: A Promising Alternative Photocatalyst for Solar Conversion. *ACS Appl. Mater. Interfaces* **2015**, *7*, 1616–1623.

(53) Yang, J.-S.; Wu, J.-J. Low-potential driven fully-depleted BiVO₄/ZnO heterojunction nanodendrite array photoanodes for photoelectrochemical water splitting. *Nano Energy* **2017**, *32*, 232–240.

(54) Ahn, K.-S.; Yan, Y.; Shet, S.; Jones, K.; Deutsch, T.; Turner, J.; Al-Jassim, M. ZnO nanocoral structures for photoelectrochemical cells. *Appl. Phys. Lett.* **2008**, *93*, No. 163117.

(55) Mao, C.; Zuo, F.; Hou, Y.; Bu, X.; Feng, P. In Situ Preparation of a Ti³⁺ Self-Doped TiO₂ Film with Enhanced Activity as Photoanode by N₂H₄ Reduction. *Angew. Chem., Int. Ed.* **2014**, *53*, 10485–10489.

(56) Chakhari, W.; Naceur, J. B.; Taieb, S. B.; Assaker, I. B.; Chtourou, R. Fe-doped TiO₂ nanorods with enhanced electrochemical properties as efficient photoanode materials. *J. Alloys Compd.* **2017**, *708*, 862–870.

(57) Liu, Q.; Ding, D.; Ning, C.; Wang, X. Reduced N/Ni-doped TiO₂ nanotubes photoanodes for photoelectrochemical water splitting. *RSC Adv.* **2015**, *5*, 95478–95487.

(58) Liu, Q.; Ding, D.; Ning, C.; Wang, X. Black Ni-doped TiO₂ photoanodes for high-efficiency photoelectrochemical water-splitting. *Int. J. Hydrogen Energy* **2015**, *40*, 2107–2114.

(59) Khan, S. U. M.; Al-Shahry, M.; Ingler, W. B., Jr. Efficient Photochemical Water Splitting by a Chemically Modified n-TiO₂. *Science* **2002**, *297*, 2243–2245.

(60) Walter, M. G.; Warren, E. L.; McKone, J. R.; Boettcher, S. W.; Mi, Q.; Santori, E. A.; Lewis, N. S. Solar Water Splitting Cells. *Chem. Rev.* **2010**, *110*, 6446–6473.

(61) Freitas, R. G.; Santanna, M. A.; Pereira, E. C. Preparation and Characterization of TiO₂ Nanotube Arrays in Ionic Liquid for Water Splitting. *Electrochim. Acta* **2014**, *136*, 404–411.

(62) Lian, Z.; Wang, W.; Xiao, S.; Li, X.; Cui, Y.; Zhang, D.; Li, G.; Li, H. Plasmonic silver quantum dots coupled with hierarchical TiO₂ nanotube arrays photoelectrodes for efficient visible-light photoelectrocatalytic hydrogen evolution. *Sci. Rep.* **2015**, *5*, No. 10461.

(63) Chen, H.; Liu, G.; Wang, L. Switched photocurrent direction in Au/TiO₂ bilayer thin films. *Sci. Rep.* **2015**, *5*, No. 10852.

(64) Giannakopoulou, T.; Papailias, I.; Todorova, N.; Boukos, N.; Liu, Y.; Yu, J.; Trapalis, C. Tailoring the energy band gap and edges' potentials of g-C₃N₄/TiO₂ composite photocatalysts for NO_x removal. *Chem. Eng. J.* **2017**, *310*, 571–580.

(65) Ai, G.; Mo, R.; Chen, Q.; Xu, H.; Yang, S.; Li, H.; Zhong, J. TiO₂/Bi₂S₃ core-shell nanowire arrays for photoelectrochemical hydrogen generation. *RSC Adv.* **2015**, *5*, 13544–13549.

(66) Ding, Y.; Nagpal, P. Titanium dioxide nanotube membranes for solar energy conversion: effect of deep and shallow dopants. *Phys. Chem. Chem. Phys.* **2017**, *19*, 10042–10050.

(67) Folli, A.; Bloh, J. Z.; Lecaplain, A.; Walker, R.; Macphee, D. E. Properties and photochemistry of valence-induced-Ti³⁺ enriched (Nb,N)-codoped anatase TiO₂ semiconductors. *Phys. Chem. Chem. Phys.* **2015**, *17*, 4849–4853.

(68) Bloh, J. Z.; Dillert, R.; Bahnemann, D. W. Ruthenium-modified zinc oxide, a highly active vis-photocatalyst: the nature and reactivity of photoactive centres. *Phys. Chem. Chem. Phys.* **2014**, *16*, 5833–5845.

(69) Li, Z.; Luo, W.; Zhang, M.; Feng, J.; Zou, Z. Photoelectrochemical cells for solar hydrogen production: current state of promising photoelectrodes, methods to improve their properties, and outlook. *Energy Environ. Sci.* **2013**, *6*, 347–370.

(70) Wang, X.; Xie, J.; Li, C. M. Architecting smart “umbrella” Bi₂S₃/rGO-modified TiO₂ nanorod array structures at the nanoscale for efficient photoelectrocatalysis under visible light. *J. Mater. Chem. A* **2015**, *3*, 1235–1242.

NOTE ADDED AFTER ASAP PUBLICATION

This paper was published on the Web on May 1, 2018, with errors in Figure 8b. The corrected version was reposted on July 11, 2018.